Title: Scheelite-type MWO_4 (M = Ca, Sr and Ba) nanophosphors: Facile synthesis, structural characterization, photoluminescence and photocatalytic properties

Author: C. Shivakumara Rohit Saraf Sukanti Behera N. Dhananjaya H. Nagabhushana

PII: S0025-5408(14)00640-0
DOI: http://dx.doi.org/doi:10.1016/j.materresbull.2014.09.096
Reference: MRB 7779

To appear in: *MRB*

Received date: 15-5-2014
Revised date: 3-9-2014
Accepted date: 26-9-2014

Please cite this article as: C.Shivakumara, Rohit Saraf, Sukanti Behera, N.Dhananjaya, H.Nagabhushana, Scheelite-type MWO4 (M = Ca, Sr and Ba) nanophosphors: Facile synthesis, structural characterization, photoluminescence and photocatalytic properties, Materials Research Bulletin http://dx.doi.org/10.1016/j.materresbull.2014.09.096

Scheelite-type MWO_4 (M = Ca, Sr and Ba) nanophosphors: Facile synthesis, structural characterization, photoluminescence and photocatalytic properties

C. Shivakumara [a,*], Rohit Saraf [b], Sukanti Behera [a], N. Dhananjaya [c], H. Nagabhushana [d]

[a] *Solid State and Structural Chemistry Unit, Indian Institute of Science, Bangalore 560012, India.*

[b] *Centre for Converging Technologies, University of Rajasthan, Jaipur 302 005, India.*

[c] *Department of Physics, B.M.S. Institute of Technology, Bangalore 560 064, India.*

[d] *C. N. R. Rao Center for Advanced Materials, Tumkur University, Tumkur 572 103, India.*

---

* Corresponding Author

C. Shivakumara. E-mail: shiva@sscu.iisc.ernet.in

Telephone : +91 80 2293 2951; FAX : +91 80 2360 1310

Highlights

- Scheelite-type MWO_4 nanphosphors were synthesized by wet chemical approach.
- CIE chromaticity diagram reveals that these nanophosphors emit intense blue luminescence.

- Under UV illumination, we achieved 100% MB dye degradation over $BaWO_4$ nanocatalysts within 60 min.
- MWO_4 can be useful in removing industrial pollutants and fabricating blue component in white LEDs.

Graphical abstract

Abstract

Scheelite-type MWO_4 (M = Ca, Sr and Ba) nanophosphors were synthesized by the precipitation method. All compounds crystallized in the tetragonal structure with space group $I4_1/a$ (No. 88). Scherrer's and TEM results revealed that the average crystallite size varies from 32 to 55 nm. FE-SEM illustrate the spherical ($CaWO_4$), bouquet ($SrWO_4$) and fish ($BaWO_4$) like morphologies. PL spectra indicate the broad emission peak maximum at 436 ($CaWO_4$), 440 ($SrWO_4$) and 433 nm ($BaWO_4$) under UV excitation. The calculated CIE color coordinates of MWO_4 nanophosphors are close to the commercial BAM and National Television System Committee blue phosphor. The photocatalytic activities of MWO_4 were investigated for the degradation of methylene blue dye under UV illumination. At pH = 3, $BaWO_4$ nanocatalyst showed 100% dye degradation within 60 min. The photocatalytic activity was in the decreasing order of $BaWO_4 > CaWO_4 > SrWO_4$ under both neutral and acidic conditions.

Keywords: A. Oxides; B. Chemical synthesis; C. X-ray diffraction; D. Phosphors; D. Catalytic properties.

1. Introduction

Alkaline-earth metal tungstates represent an important class of inorganic materials [1, 2]. These metal tungstates have a scheelite-type tetragonal structure with space group *I41/a* (No. 88) and point group C^{6}_{4h} symmetry [3]. In the scheelite structure, alkaline earth metal ions coordinated with eight oxygen atoms and tungstate ions were connected with four oxygen atoms in the tetrahedral symmetry. These class of oxides have a wide range of technological applications as acousto-optic filters [4], solid state lasers [5, 6], light emitting diodes [7], photocatalysts [8, 9], phosphors [10, 11, 12, 13] and cryogenic scintillation detectors [14]. The scheelite-type tungstates exhibit self luminescence in almost entire visible spectrum which could be decomposed in blue, green and red components. The emission in blue region was assigned to the charge transfer transition within WO_4^{2-} group [15]. Campos et al. [16, 17] showed that green luminescence can be attributed to both oxygen complex vacancies and intrinsic slight distortion. However, the position of emission peak was shown to be a function of the synthesis method (i.e. morphology and particle size) and excitation wavelength. The excitation using shorter wavelength (210–280 nm) gives blue emission, while longer wavelengths yield green and red emission [18].

During the last three decades semiconductor metal oxides have been extensively used for their photocatalytic activity, because of their advantages such as higher efficiency of generation, mobility and separation of photoinduced electrons and holes, low cost and environmental friendliness. As a well-known semiconductor, TiO_2 has proven photocatalytic activity for oxidative decomposition of organic compounds. Nevertheless, TiO_2 was hampered by both inherent slow reaction rates and poor solar efficiency in solar radiation. Several doped materials have better photocatalytic performance, while the activity of TiO_2 was rather limited [19]. Recently, some alternative oxide materials like tantalites, vanadates, molybdates, niobates, and

tungstates have been investigated for their photocatalytic activity towards water splitting and organic pollutants degradation. In spite of some progress, achieving high photocatalytic activity in the oxide semiconductors still remains a great challenge.

Several techniques have been employed to synthesize metal tungstates, such as the conventional solid state reaction [20], solvothermal [21], hydrothermal [22], spray pyrolysis [23], sol–gel [24], surfactant-assisted precipitation [25], galvanic [26, 27], microwave irradiation [28], pulsed laser deposition [29] and vapor-deposited [30] method. All these methods require high temperature, long processing time and sophisticated equipment with high maintenance costs. They also lead to the formation of deleterious phases. However, room temperature precipitation method was convenient, economical, energy saving, environmentally friendly and less time consuming as compared to conventional preparative methods.

In the present work, scheelite-type metal tungstates nanophosphors were synthesized by wet chemistry approach at room temperature. These nanophosphors were characterized using powder X-ray diffraction (XRD), Field emission Scanning electron microscopy (FE-SEM), Transmission electron microscopy (TEM), Fourier transform infrared (FTIR) and UV–Visible spectroscopy. Further, the photoluminescence and photocatalytic activity were carried out for possible energy saving and environmental remedy applications.

2. Experimental

2.1. Materials

$Ca(NO_3)_2.4H_2O$, $Sr(NO_3)_2$, $Ba(NO_3)_2$, $Na_2WO_4.2H_2O$ and Methylene blue dye were analytical reagent grade and used without further purification.

2.2. Synthesis

MWO_4 (M = Ca, Sr and Ba) compounds were prepared by the precipitation method at room temperature without using any surfactant or stabilizing agent. In a typical synthesis of $CaWO_4$ compound, stoichiometric amount of $Ca(NO_3)_2.4H_2O$ (0.1 mol) and $Na_2WO_4.2H_2O$ (0.1 mol) were dissolved in 100 ml distilled water separately. The calcium nitrate solution was added dropwise into the sodium tungstate solution with constant stirring for 1 h and the resulting white suspension was aged for 2 h. The chemical reaction between calcium nitrate and sodium tungstate in aqueous medium is as follows:

$$Ca(NO_3)_2.4H_2O + Na_2WO_4.2H_2O \rightarrow CaWO_4 + 2NaNO_3 + 6H_2O \quad (1)$$

Finally, the white precipitate was washed with distilled water for several times, filtered and dried at 100 °C for 2 h. Similarly, $SrWO_4$ and $BaWO_4$ were synthesized by choosing $Sr(NO_3)_2$ and $Ba(NO_3)_2$ as starting materials.

2.3. Characterization

The phase purity of MWO_4 powder was examined by powder X-ray diffraction (XRD) (PANalytical X'Pert Pro Powder diffractometer) using Cu Kα radiation (λ = 1.5418 Å, Ni filter). For Rietveld refinement, data were collected at a scan rate of 2˚/ min (0.02˚ step size for 2θ from 10˚ to 80˚). Refinement was done using FullProf Suite-2000 version. Fourier transform infrared (FTIR) spectra were recorded by Perkin Elmer Spectrometer, Frontier using KBr as a reference. The surface morphology and crystallite size were examined using FE-SEM (FEI Sirion XL 30) at accelerating voltage of 10 kV and TEM (JEOL 2100F microscope operated at 200 kV). UV–Visible absorption spectra have been recorded for powders on Perkin Elmer Lambda 750 spectrophotometer. The photoluminescence studies have been carried out using Perkin Elmer Luminescence Spectrometer (LS-55). The photocatalytic activity of methylene blue (MB)

solutions was analyzed by a Perkin Elmer UV – Visible spectrophotometer (Lambda 35) in the range from 200 to 800 nm periodically.

2.4. Photocatalytic activity measurement

The photocatalytic performance of MWO_4 nanocatalysts were evaluated by decomposing the methylene blue under UV light irradiation at room temperature. In a typical dye degradation experiment, about 50 mg of MWO_4 nanocatalysts were dropped into the 50 ml of aqueous solution of MB (1×10^{-5} M) to form suspension. Mercury - vapor lamp (125 W, Philips) was used as the UV light source (λ = 365 nm). Prior to UV illumination, the suspension was continuously stirred for about 30 minutes in the dark to develop adsorption – desorption equilibrium between MB dye and the catalyst. Then, the stable aqueous suspension was exposed to UV light from 0 to 60 minutes. During the photoreaction, about 3 ml of suspension was collected at different time and centrifuged to remove the catalyst. The clear suspension was analyzed using UV-Visible spectrophotometer. The percentage dye degradation rate was calculated by the following equation [31]:

$$\text{Photodegradation rate} = \frac{C_0 - C}{C_0} \times 100 \qquad (2)$$

where C_0 is the initial concentration at 0 min and C is the concentration at time t.

3. Results and discussion

3.1. Powder X-ray diffraction

Indexed powder X-ray diffraction patterns for MWO_4 (M = Ca, Sr and Ba) compounds were shown in Fig. S1. All the diffracted lines were agreed well with the JCPDS File Nos. 85-

0854 ($CaWO_4$), 85-0587 ($SrWO_4$) and 85-0588 ($BaWO_4$). We did not observe any deleterious diffracted lines; this confirms that all the compounds were single phase. The XRD peaks shifted towards lower 2θ angles from $CaWO_4$ to $BaWO_4$ phosphors due to the increase in ionic radii of 8 - coordinated alkaline earth metal ions, Ca (r_{Ca}^{2+} = 1.12 Å), Sr (r_{Sr}^{2+} = 1.26 Å) and Ba (r_{Ba}^{2+} = 1.42 Å). The structural parameters were obtained from the Rietveld refinement method using powder XRD data. The patterns were typically refined for lattice parameters, scale factor, backgrounds, pseudo-Voigt profile function (u, v and w), atomic coordinates and isothermal temperature factors (B_{iso}). The refinement result reveals that all the compounds crystallized in the tetragonal scheelite-structure with space group $I4_1/a$ (No. 88). The observed, calculated and the difference XRD patterns for MWO_4 compounds were shown in Fig. 1. There was a good agreement between the observed and calculated patterns. In Table 1, we have summarized the refined structural parameters for MWO_4 compounds. The lattice parameters (*a*, *c*) and unit cell volume increase with increasing ionic radii of alkaline earth ions (Fig. S2). The crystal structure of MWO_4 was modeled through VESTA program [33] using structural parameters obtained from Rietveld method. In MWO_4 structure (Fig. 2), the alkaline earth (M) atoms were coordinated to eight oxygen (O) atoms having two types of M – O distances, which results in deltahedral [MO_8] clusters. The tungsten (W) atoms were coordinated to four oxygen atoms which form [WO_4] clusters. These [WO_4] clusters were slightly distorted in the lattice due to difference in the O – W – O bond angles. From Table 1, W – O bond lengths decrease with increasing ionic radii of M ions. Whereas, M – O' and M – O" increase with increasing ionic radii of M ions. On the other hand, M – O – M, M – O' – W bond angles decrease and M – O" – W increase with increasing ionic radii of M ions.

The average crystallite size was estimated using Scherrer's equation [34]:

$$D = \frac{k\lambda}{\beta \cos\theta} \tag{3}$$

where λ is the wavelength (1.5418 Å) of X-rays, β is the full width at half maximum (FWHM), θ is the diffraction angle, k is the shape factor (0.9) and D is the average crystallite size. Based on this equation, the average crystallite sizes for $CaWO_4$, $SrWO_4$ and $BaWO_4$ powders were found to be 32, 33 and 55 nm, respectively. The broadening of the XRD lines decrease with increasing crystallite sizes. The effects of the lattice strain and crystallite size on the FWHM were estimated by Williamson and Hall (W–H) plots using the relation [35]:

$$\beta \cos\theta = \frac{k\lambda}{D} + 4\varepsilon \sin\theta \tag{4}$$

where λ is the wavelength of X-rays (1.5418 Å), β (FWHM in radians) is measured for different XRD lines corresponding to different planes, θ is the diffraction angle, k is the shape factor (0.9), D is the crystallite size and ε is the micro strain. For estimation of lattice strain, βcosθ was plotted against 4sinθ (Fig. S3). The slope of line gives the strain (ε) and intercept (kλ/D) on Y-axis gives crystallite size (D). The lattice strain increases with increasing broadening of the X-ray diffraction line (Table 2). The crystallite size calculated from W–H plots for MWO_4 was in good agreement with those obtained from Scherrer's method. This reveals that the compounds were nanocrystalline in nature. The plot has a near zero slope for $BaWO_4$ showing minimal or no contribution due to strain.

3.2. FE-SEM and TEM analysis

Fig. 3 shows FE-SEM images of MWO_4 compounds obtained from precipitation method at room temperature. The $CaWO_4$ nanospheres processed in an aqueous medium exhibited an average size distribution in the range from 25–50 nm (Fig. 3a). Fig. 3b illustrates the uniform

$CaWO_4$ microspheres, with an average diameter of 5 μm, which comprise of agglomerated nanoparticles. In Fig. 3d, the FESEM image revealed bouquet-like $SrWO_4$ microcrystals with an average size of about 3 μm, which were also composed of small spherical nanoparticles with the size of 30–70 nm (Fig. 3c). Fig. 3e shows the morphology of aggregation of small nanocrystals lead to the formation of fish-like microcrytals (Fig. 3f). These micrographs suggest that the chemical reaction between alkaline earth metal and tungstate ions leads to fast nucleation, growth and agglomeration of small particles. Fig. 4 shows the TEM images of MWO_4 compounds. From Fig. 4, the nanoparticles were obtained in the range of 30–40 nm ($CaWO_4$), 35–45 nm ($SrWO_4$) and 50–60 nm ($BaWO_4$), which was consistent with the calculated values of the average crystallite size obtained from the Scherrer's and W-H methods.

3.3. FTIR studies

For the alkaline earth tungstate MWO_4 with scheelite structure, there are 26 different vibration modes which are represented by the following equation:

$$\Gamma = 3A_g + 5A_u + 5B_g + 3B_u + 5E_g + 5E_u \quad (5)$$

All even vibrations A_g, B_g and E_g are Raman-active modes, while the odd modes $4A_u$ and $4E_u$ are active only in infrared frequencies and remaining five vibrations [$1A_u$ and $1E_u$ are acoustic modes and 3 B_u are forbidden] are IR inactive modes [36, 37].

The FTIR spectra (Fig. 5) of MWO_4 nanophosphors measured in the wave number region of 350–2000 cm^{-1}. The characteristic strong and broad absorption bands have two vibration modes around 800 cm^{-1} ($CaWO_4$), 808 cm^{-1} ($SrWO_4$), and 820 cm^{-1} ($BaWO_4$) were related to ν_3[($1E_u$) and ($1A_u$)] internal modes which were assigned to O–W–O anti-symmetry stretching vibrations in [WO_4] tetrahedron. A sharp but less intense absorption peaks at 438 cm^{-1} ($CaWO_4$),

410 cm^{-1} ($SrWO_4$), and 380 cm^{-1} ($BaWO_4$) have appeared, which arises due to symmetric bending vibrational mode $\nu_4[1(A_u + E_u)]$ within the [WO_4] tetrahedron. Adsorbed water molecules on the surface of the sample at 1631 cm^{-1}, 1631 cm^{-1} and 1617 cm^{-1} were also detected for $CaWO_4$, $SrWO_4$ and $BaWO_4$ respectively. The photocatalytic activity was closely related to the number of –OH groups present on the surface of catalyst because the photogenerated holes (h^+) react with water and generate •OH radicals, which can oxidize the organic pollutants. Therefore, an increase in the number of surface –OH groups could improve the photocatalytic activity.

3.4. UV-Visible absorption spectroscopy

The UV-Vis absorption spectra of MWO_4 nanophosphors (Fig. 6a) indicate a blue-shift of the UV−Visible absorption edges with increasing ionic radii of M ions. $CaWO_4$, $SrWO_4$ and $BaWO_4$ nanophosphors have intense absorption edges at 290, 266 and 259 nm which lie in the UV region. The optical band gap energy (E_g) was estimated by the method proposed by Wood and Tauc. The optical band gap was calculated with absorbance and photon energy by the following equation [38]:

$$\alpha h\nu = A\left(h\nu - E_g\right)^n \tag{6}$$

where α = Absorption coefficient, $h\nu$ = Photon energy, E_g = Band gap energy, A is a constant that is different for different types of transitions, indicated by different values of n (n = 1/2, 2, 3/2, or 3 for allowed direct, allowed indirect, forbidden direct, and forbidden indirect electronic transitions, respectively). Fig. 6b depicts the plots of $(\alpha h\nu)^2$ versus the photon energy ($h\nu$) for MWO_4 nanophosphors. The intercept of the tangent to the x-axis gives good approximation of the band gap energies of $CaWO_4$, $SrWO_4$ and $BaWO_4$ nanophosphors as 4.27, 4.66, and 4.79 eV, respectively. These band gap energy values nearly matched with the literature

[39, 40] (Table 2). It was clearly seen that the band gap energy increases with increasing ionic radii of M ions.

3.5. Photoluminescence properties

Photoluminescence spectra were often used to examine the efficiency of charge carrier trapping, immigration and transfer, as well as to understand the fate of photogenerated e^-/h^+ pairs in semiconductor particles. Fig. 7 exhibits the excitation spectra of $CaWO_4$, $SrWO_4$ and $BaWO_4$ nanophosphors, which shows the broad band with a maximum at 350, 355 and 350 nm, when monitored at 436, 440 and 433 nm emission wavelengths, respectively. For $CaWO_4$, an intrinsic broad emission peak was observed centered at 436 nm upon excitation at 350 nm (Fig. 7a). In case of $SrWO_4$ (λ_{ex} = 375 nm), the emission peak was highest at 440 nm (Fig. 7b). The emission spectrum of $BaWO_4$ nanophosphor shown in Fig. 7c revealed the peak at 433 nm under excitation of 350 nm. It was generally accepted that the excitation and emission of MWO_4 nanophosphors mainly arise from the charge-transfer transitions from the oxygen ligands to the central tungsten atom within the WO_4^{2-} complex between the last fully occupied t_1 orbital and the first empty 2e orbital [26, 41].

The broad band suggests that the emission process was a typical multi phonon or multi level process, i.e., a solid system in which the relaxation occurs by several paths, involving the participation of numerous energy states within the band gap. It can be observed that MWO_4 emission curves exhibit a broad luminescence in the blue wavelength range. The excitation from the ground state ($^1A_1$) of WO_4^{2-} gives rise to four excited states, i.e., $^1T_2$, $^1T_1$, $^3T_2$, and $^3T_1$, from which only the transition between $^1A_1$ and $^1T_2$ is electric dipole allowed [42]. However, the WO_4^{2-} complexes in scheelite tungstates are slightly distorted from T_d to D_{2d} symmetry by the influence of the Jahn-Teller effect and electron-phonon interactions in general [43, 44]. Hence,

the orbitally degenerate T state undergoes distortion and symmetry lowering to a D_{2d} symmetry state, which strongly enhances the number of transitions observed. Both $^1A_1 \rightarrow {}^1T_2$, $^1T_1$ and $^1A_1 \rightarrow {}^3T_2$, $^3T_1$ transitions become partially allowed, thereby rendering radiative transitions from low-lying triplet excited states to the $^1A_1$ ground state as clearly detectable emission peaks (i.e., at 437 nm) in the blue luminescent spectra.

The color clarity of any luminescent material was expressed in terms of chromaticity coordinates, called Commission International De I'Eclairage (CIE). The CIE chromaticity coordinates (x, y) were calculated from the PL spectra. Fig. 8 shows the CIE chromaticity diagram of MWO_4 nanophosphors. The CIE coordinates of $CaWO_4$, $SrWO_4$ and $BaWO_4$ were found to be (0.150, 0.056), (0.149, 0.076) and (0.151, 0.059), respectively, which fall into the blue region of the CIE diagram. The evaluated color coordinates are close to the commercial BAM (0.144, 0.072) and National Television System Committee (NTSC) blue phosphor (0.140, 0.080) [45]. Therefore, the present nanophosphors can be useful for the production of blue component in white LEDs.

3.6. Photocatalytic activity

Methylene Blue was a cationic dye and releases MB^+ ions on dissolution in water, absorbing the light in the 500–700 nm range. The MB dye degradation was demonstrated at neutral (pH = 7) and acidic (pH = 3) conditions over MWO_4 nanocatalysts under UV illumination. UV–Vis spectra of decomposed MB dye with the variation of time from 0 to 60 min exhibits the maximum absorption wavelength at 664 nm (Fig. S4). Under both neutral and acidic conditions, the absorbance intensities of MB were gradually decreased in the presence of MWO_4 nanocatalysts with time.

At pH = 7, when the reaction was performed under dark for 30 min, we observed 57%, 30%, and 27% MB dye degradation for $BaWO_4$, $CaWO_4$, and $SrWO_4$ nanocatalysts respectively (Figs. S5a, 9a). However, there was a negligible change in MB dye concentration in acidic condition (Figs. S5b, 9b). Under neutral condition, MB dye was significantly degraded by 88%, 85%, and 54% within 60 minutes for $BaWO_4$, $CaWO_4$, and $SrWO_4$ nanocatalysts respectively. In case of acidic condition, 100% dye degradation was observed over $BaWO_4$ within 60 min which was higher than 94% for $CaWO_4$ and 74% for $SrWO_4$. This implies that acidic conditions were favorable towards the formation of the reactive intermediates that is hydroxyl radicals was significantly enhanced, which further help in enhancing the reaction rate. On the other hand in neutral medium conditions, the formation of reactive intermediates was relatively less favourable and hence less spontaneous.

The pH-dependent photodegradation can be mainly attributed to the variations of surface charge properties of the photocatalyst. Consequently, this changes the absorption behavior of a dye on the catalyst surface. The differences in the photocatalytic activity in synthesized tungstates can be ascribed to different factors, such as the amount of adsorbed dyes, the position of the valence and conductive bands and the rate of the electron–hole recombination. The good results of photocatalytic activity were obtained in the decreasing order of $BaWO_4$ > $CaWO_4$ > $SrWO_4$ under both neutral and acidic conditions.

The kinetics of MB degradation reaction was presented in Fig. 10, which follows apparent first order kinetics in agreement with a general Langmuir–Hinshelwood mechanism [46]:

$$R = \frac{-dC}{dt} = \frac{kKC}{1+KC} \tag{7}$$

where R is the degradation rate of reactant (mg/l min), C is the concentration of reactant (mg/l), t the illumination time, K is the adsorption coefficient of reactant (l/mg) and k is the reaction rate constant (mg/l min). If C is very small then the above equation could be simplified to

$$\ln\left(\frac{C_0}{C}\right) = kKt = k_{app}t \quad (8)$$

where C_0 is the initial concentration (0 min) of the MB aqueous solution and C is the concentration of the MB aqueous solution for different times of UV illumination.

From the plot of $\ln(C_0/C)$ vs. the irradiation time (t) (Fig. 10a), straight lines can be fitted in the first part of the plots, allowing to estimate apparent first order kinetic constants of 0.029 min^{-1} ($BaWO_4$), 0.026 min^{-1} ($CaWO_4$) and 0.07 min^{-1} ($SrWO_4$) under neutral conditions. We have noted that this rate constant values are smaller than the values k_{BaWO4} = 0.086 min^{-1}, k_{CaWO4} = 0.044 min^{-1}, and k_{SrWO4} = 0.022 min^{-1} for the degradation of MB dye under acidic condition (Fig. 10b). As the decolorization reactions proceed, the reaction rates significantly deviate from the straight line, suggesting that the presence of adsorbed intermediates and products of the complete mineralization adsorbed on the photocatalysts surface affects the process. For instance, formation of carbonates from the interaction with the CO_2 produced from dyes degradation was previously indicated as major drawback of active Bi_2O_3 photocatalyst [47]. Further, we have also compared our photocatalytic results with the reported catalysts for the degradation of MB dye and were shown in Table 3. The table reveals that $BaWO_4$ nanocatalyst shows 100% MB dye degradation in shorter duration (60 min.) and its rate constant under acidic condition is higher as compared to TiO_2 [48], 5% Ag-ZnO [49], SnO_2: Zn^{2+} [50] and $ZnWO_4$ [51] catalysts.

When the energy of UV light in terms of photon is equal to or greater than the band gap of MWO_4, the electrons receive energy and transfer of electrons takes place from the valence band (VB) to the conduction band (CB) which result in the formation of a hole (h^+) in the VB and an electron (e^-) in the CB. The holes react with water and generate •OH radicals, which can oxidize the organic pollutants. The conduction band electron reacts with oxygen in the reduction process and produces •OH radicals. These radicals reduce the organic pollutants. These oxidation and reduction processes were capable of degrading the organic pollutants under UV light irradiation. According to this, the relevant reactions at the semiconductor surface causing the degradation of MB dye can be expressed as follows:

$$MWO_4 + h\nu\ (UV) \rightarrow MWO_4\ (e_{CB}^- + h_{VB}^+) \quad (9)$$

$$MWO_4\ (h_{VB}^+) + H_2O \rightarrow MWO_4 + H^+ + \bullet OH \quad (10)$$

$$MWO_4\ (h_{VB}^+) + OH^- \rightarrow MWO_4 + \bullet OH \quad (11)$$

$$MWO_4\ (e_{CB}^-) + O_2 \rightarrow MWO_4 + \bullet O_2^-\ (\text{or } \bullet O^-) \quad (12)$$

$$\bullet O_2^-\ (\text{or } \bullet O^-) + H^+ \rightarrow \bullet O_2H\ (\text{or } \bullet OH) \quad (13)$$

$$C_{16}H_{18}N_3SCl + \bullet OH \rightarrow CO_2, NH_4^+, NO_3^-, SO_4^{2-}, Cl^- \text{ and } H_2O \quad (14)$$

$$C_{16}H_{18}N_3SCl + h_{VB}^+ \rightarrow \text{oxidation products} \quad (15)$$

$$C_{16}H_{18}N_3SCl + e_{CB}^- \rightarrow \text{reduction products} \quad (16)$$

where *hν* is photon energy required to excite the semiconductor electron from the valence band (VB) region to conduction band (CB) region.

4. Conclusions

MWO_4 (M = Ca, Sr and Ba) nanophosphors were synthesized by the room temperature precipitation method. Powder XRD and Rietveld refinement data indicate that these

nanophosphors have a monophasic scheelite-type tetragonal structure. FE-SEM images of $CaWO_4$, $SrWO_4$ and $BaWO_4$ nanophosphors suggest the spherical, bouquet and fish-like morphology, respectively. PL spectra exhibit the broad intense blue emission peak. It was observed that the measured CIE coordinates of MWO_4 nanophosphors are close to the commercial BAM (0.144, 0.072) and NTSC blue phosphor (0.140, 0.080). At pH = 3, 100% MB dye degradation was observed within 60 minutes over $BaWO_4$ nanocatalysts under UV illumination.The photocatalytic activity was in the decreasing order of $BaWO_4$ > $CaWO_4$ > $SrWO_4$ under both neutral and acidic conditions. All these results indicate that MWO_4 is a promising candidate for the development of blue phosphor in white LEDs as well as for removing industrial pollutants.

Acknowledgements

The authors like to thank Mr. Surender Kumar, IPC for providing solid UV-Visible data and acknowledge for chemical division TEM facility, IISc. One of the authors (R.S.) greatly acknowledges Professor Ashok K. Nagawat and Dr. K.V.R. Rao, Centre for Converging Technologies, University of Rajasthan for encouragement.

References

[1] N. Saito, N. Sonoyama, T. Sakata, Bulletin of the Chemical Society of Japan 69 (1996) 2191– 2194.

[2] H.W. Liao, Y.F. Wang, X.M. Liu, Y.D. Li, Y.T. Qian, Chemistry of Materials 12 (2000) 2819–2821.

[3] G. Wan, G. Wang, Modern Physics Letters B 24 (2010) 3081 – 3087.

[4] V.I. Balakshy, K.R. Asratyan, V.Y. Molchanov, Journal of Optics A- Pure and Applied Optics 3 (2001) S87–S92.

[5] L. Fan, Y.X. Fan, Y.H. Duan, Q. Wang, H.T. Wang, G.H. Jia, C.Y. Tu, Applied Physics B-Lasers and Optics 94 (2009) 553–557.

[6] J. Sulc, H. Jelinkova, T.T. Basiev, M.E. Doroschenko, L.I. Ivleva, V.V. Osiko, P.G. Zverev, Optical Materials 30 (2007) 195–197.

[7] P.G. Yang, J. Liu, H. Yang, X. Yu, Y. Guo, Y. Zhou, J. Liu, Journal of Materials Chemistry 19 (2009) 3771–3774.

[8] J. Bi, L. Wu, Y. Zhang, Z. Li, J. Li, X. Fu, Applied Catalysis B- Environmental 91 (2009) 135–143.

[9] J. Yu, L. Qi, B. Cheng, X. Zhao, Journal of Hazardous Materials 160 (2008) 621–628.

[10] A.K. Parchur, R.S. Ningthoujam, Dalton Transactions 40 (2011) 7590–7594.

[11] J. Liao, B. Qiu, H. Wen, J. Chen, W. You, Materials Research Bulletin 44 (2009) 1863–1866.

[12] D. Gao, Y. Li, X. Lai, Y. Wei, J. Bi, Y. Li, M. Liu, Materials Chemistry and Physics 126 (2011) 391–397.

[13] A.K. Parchur, A.I. Prasad, A.A. Ansari, S.B. Rai, R.S. Ningthoujam, Dalton Transactions 41 (2012) 11032–11045.

[14] H. Kraus, V.B. Mikhailik, Nuclear Instruments and Methods in Physics Research Section A-Accelerators Spectrometers Detectors and Associated Equipment 621 (2010) 395–400.

[15] H. Wang, F.D. Medina, D.D. Liu, Y.D. Zhou, Journal of Physics: Condensed Matter 6 (1994) 5373–5386.

[16] A.B. Campos, A.Z. Simoes, E. Longo, J.A. Varela, V.M. Longo, A.T. de Figueiredo, F.S. De Vicente, A.C. Hernandes, Applied Physics Letters 91 (2007) 051923– 051923-3.

[17] V.M. Longo, A.T. Figueiredo, A.B. Campos, J.W.M. Espinosa, A.C. Hernandes, C.A. Taft, J.R. Sambrano, J.A. Varela, E. Longo, The Journal of Physical Chemistry A 112 (2008) 8920–8928.

[18] L. Ma, Y. Sun, P. Gao, Y. Yin, Z. Qin, B. Zhou, Materials Letters 64 (2010) 1235–1237.

[19] T. Yan, L. Li, W. Tong, J. Zheng, Y. Wang, G. Li, Journal of Solid State Chemistry 184 (2011) 357–364.

[20] G. Blasse, L.H. Brixner, Chemical Physics Letters 173 (1990) 409–411.

[21] D. Chen, G. Shen, K. Tang, H. Zheng, Y. Qian, Materials Research Bulletin 38 (2003) 1783–1789.

[22] X. Lai, Y. Wei, D. Qin, Y. Zhao, Y. Wu, D. Gao, J. Bi, D. Lin, G. Xu, Integrated Ferroelectrics 140 (2012) 177–186.

[23] Z. Lou, M. Cocivera, Materials Research Bulletin 37 (2002) 1573–1582.

[24] P.Y. Jia, X.M. Liu, G.Z. Li, M. Yu, J. Fang, J. Lin, Nanotechnology 17 (2006) 734–742.

[25] X. Lai, Y. Wei, D. Qin, Y. Zhao, Y. Wu, D. Gao, J. Bi, D. Lin, G. Xu, Integrated Ferroelectrics 142 (2013) 7–15.

[26] J. Bi, C.H. Cui, X. Lai, F. Shi, D.J. Gao, Materials Research Bulletin 43 (2008) 743–747.

[27] D. Gao, X. Lai, C. Cui, P. Cheng, J. Bi, D. Lin, Thin Solid Films 518 (2010) 3151–3155.

[28] J.H. Ryu, J.W. Yoon, K.B. Shim, Electrochemical and Solid-State Letters 8 (2005) D15–D18.

[29] K. Tanaka, K. Fukui, K. Ohga, C.K. Choo, Journal of Vacuum Science and Technology A 20 (2002) 486–491.

[30] P.F. Carcia, M. Reilly, C.C. Torardi, M.K. Crawford, C.R. Miao, B.D. Jones, Journal of Materials Research 12 (1997) 1385–1390.

[31] S.A. Khayyat, M.S. Akhtar, A. Umar, Materials Letters 81 (2012) 239–241.

[32] R.D. Shannon, Acta Crystallographica Section A 32 (1976) 751–767.

[33] K. Momma, F. Izumi, Journal of Applied Crystallography 41 (2008) 653−658.

[34] P. Klug, L.E. Alexander, X-ray Diffraction Procedure, Wiley, New York, 1954.

[35] G.K. William, W.H. Hall, Acta Metallurgica 1 (1953) 22–31.

[36] L.S. Cavalcante, J.C. Sczancoski, L.F. Lima, J.W.M. Espinosa, P.S. Pizani, J.A. Varela, E. Longo, Crystal Growth and Design 9 (2009) 1002–1012.

[37] A. Phuruangrat, T. Thongtem, S. Thongtem, Superlattices and Microstructures 52 (2012) 78–83.

[38] J. Tauc, Optical Properties of Solids, North-Holland, Amsterdam, 1970.

[39] S.K. Arora, B. Chudasama, Crystal Research and Technology 41 (2006) 1089–1095.

[40] R. Lacomba-Perales, J. Ruiz-Fuertes, D. Errandonea, D. Martinez-Garcia, A. Segura, Europhysics Letters 83 (2008) 37002–37002-5.

[41] R. Grasser, A. Scharmann, Journal of Luminescence 12/13 (1976) 473–478.

[42] F. Zhang, M.Y. Sfeir, J.A. Misewich, S.S. Wong, Chemistry of Materials 20 (2008) 5500–5512.

[43] K. Polak, M. Nikl, K. Nitsch, M. Kobayashi, M. Ishii, Y. Usuki, O. Jarolimek, Journal of Luminescence 72-74 (1997) 781–783.

[44] M. Nikl, P. Bohacek, E. Mihokove, M. Kobayashi, M. Ishii, Y. Usuki, V. Babin, A. Stolovich, S. Zazubovich, M. Bacci, Journal of Luminescence 87-89 (2000) 1136–1139.

[45] W.R. Liu, C.H. Huang, C.P. Wu, Y.C. Chiu, Y.T. Yeh, T.M. Chen, Journal of Materials Chemistry 21 (2011) 6869–6874.

[46] D.F.Ollis, The Journal of Physical Chemistry B 109 (2005) 2439−2444.

[47] J. Eberl, H. Kisch, Photochemical and Photobiological Sciences 7 (2008) 1400–1406.

[48] S. Senthilkumaar, K. Porkodi, R. Vidyalakshmi, Journal of Photochemistry and Photobiology A: Chemistry 170 (2005) 225–232.

[49] M.J. Height, S.E. Pratsinis, O. Mekasuwandumrong, P. Praserthdam, Applied Catalysis B: Environmental 63 (2006) 305–312.

[50] L. Li, J. Liu, Y. Su, G. Li, X. Chen, X. Qiu, T. Yan, Nanotechnology 20 (2009) 155706 (9pp).

[51] T. Montini, V. Gombac, A. Hameed, L. Felisari, G. Adami, P. Fornasiero, Chemical Physics Letters 498 (2010) 113–119.

Figure Captions

Fig. 1. Observed, calculated and the difference XRD patterns for (a) $CaWO_4$, (b) $SrWO_4$ and (c) $BaWO_4$ compounds.

Fig. 2. Crystal structures of MWO_4 (M = Ca, Sr and Ba) nanophosphors.

Fig. 3. FE-SEM images of (a, b) $CaWO_4$, (c, d) $SrWO_4$ and (e, f) $BaWO_4$ nanophosphors.

Fig. 4. TEM images of (a) $CaWO_4$, (b) $SrWO_4$ and (c) $BaWO_4$ nanophosphors.

Fig. 5. FTIR spectra of (a) $CaWO_4$, (b) $SrWO_4$ and (c) $BaWO_4$ nanophosphors.

Fig. 6. (a) UV−Vis absorption spectra and (b) plots of $(\alpha h\nu)^2$ versus the photon energy ($h\nu$) of $CaWO_4$, $SrWO_4$ and $BaWO_4$ nanophosphors.

Fig. 7. Excitation and emission spectra of (a) $CaWO_4$, (b) $SrWO_4$ and (c) $BaWO_4$ nanophosphors.

Fig. 8. CIE chromaticity diagram of $CaWO_4$, $SrWO_4$ and $BaWO_4$ nanophosphors.

Fig. 9. Relative concentration variation of MB over $BaWO_4$, $SrWO_4$ and $CaWO_4$ nanocatalysts under (a) pH = 7 and (b) pH=3 with irradiation time.

Fig. 10. First order kinetics of MB dye degradation as a function of time over $BaWO_4$, $SrWO_4$ and $CaWO_4$ nanocatalysts (a) pH = 7 and (b) pH=3.

Supplementary Figure Captions

Fig. S1. XRD patterns of (a) $CaWO_4$, (b) $SrWO_4$ and (c) $BaWO_4$ nanophosphors.

Fig. S2. Plots of (a) lattice parameters and (b) cell volumes as a function of alkaline earth ions.

Fig. S3. W–H plots of (a) $CaWO_4$, (b) $SrWO_4$ and (c) $BaWO_4$ nanophosphors.

Fig. S4. UV–Vis absorbance spectra of MB dye as a function of time and pH over (a, b) $BaWO_4$, (c, d) $SrWO_4$ and (e, f) $CaWO_4$ nanocatalysts under UV illumination.

Fig. S5. Percentage of MB dye degradation over $CaWO_4$, $SrWO_4$, and $BaWO_4$ nanocatalysts under (a) pH = 7, and (b) pH=3 as a function of irradiation time.

Table 1. Rietveld refined structural parameters, selected bond lengths and bond angles for $CaWO_4$, $SrWO_4$ and $BaWO_4$ nanophosphors.

Compounds	$CaWO_4$	$SrWO_4$	$BaWO_4$
Crystal System	Tetragonal	Tetragonal	Tetragonal
Space group	$I4_1/a$ (No. 88)	$I4_1/a$ (No. 88)	$I4_1/a$ (No. 88)
Lattice Parameters (Å)			
a	5.250(1)	5.421(5)	5.615(2)
c	11.393(3)	11.952(9)	12.722(4)
Cell volume ($Å^3$)	314.03(11)	351.27(6)	401.04(3)
Atomic positions*			
M (4b)			
x	0.0000	0.0000	0.0000
y	0.2500	0.2500	0.2500
z	0.6250	0.6250	0.6250
W (4a)			
x	0.0000	0.0000	0.0000
y	0.2500	0.2500	0.2500
z	0.1250	0.1250	0.1250
O (16f)			
x	0.2752(3)	0.2683(2)	0.2422(2)
y	0.0964(5)	0.1093(2)	0.1403(3)
z	0.0440(6)	0.0496(7)	0.0369(9)
$R_{\textbf{Factors}}$			
R_p	2.73	3.38	5.39
R_{wp}	3.57	4.16	7.28
R_{exp}	6.51	6.58	7.39
χ^2	0.30	0.40	0.97
R_{Bragg}	2.23	3.76	7.56
R_F	3.24	5.22	9.46
Bond lengths (Å)*	1.894 (6)	1.873 (3)	1.846 (4)
W – O x 4	2.356 (3)	2.487 (8)	2.619 (2)
M – O' x 4	2.398 (1)	2.552 (3)	2.842 (3)
M – O" x 4	109.12 (5)	106.37 (3)	101.86 (2)
Bond angles (°)*	121.31 (4)	122.46 (3)	114.04 (2)
M – O – M	128.55 (7)	130.82 (4)	143.04 (1)
M – O' – W	103.73 (1)	103.38 (7)	107.91 (1)
M – O" – W	121.70 (2)	122.49 (6)	110.26 (6)
O' – W – O'			
O" – W – O"			

*__Table 2.__ Crystallite size, lattice strain and energy band gap of $CaWO_4$, $SrWO_4$ and $BaWO_4$ nanophosphors.

Compounds	Crystallite size (nm)		Lattice strain (10^{-4})	Band gap (E_g) (eV)	
	Scherrer's	W – H		Present work	Literatures [39, 40]
$CaWO_4$	32	34	7.5	4.27	4.2 – 6.8
$SrWO_4$	33	32	4.2	4.66	4.5 – 4.9
$BaWO_4$	55	57	1.8	4.79	4.7 – 5.2

Table 3. Comparison of MWO_4 (M = Ca, Sr and Ba) with the reported catalysts for MB dye degradation.

Catalyst	Crystallite Size (nm)	Initial MB conc.	Catalyst conc. (mg/L)	Reaction condition	MB degradation		Rate constant (min^{-1})	Reference
					Percentage	Time taken (min.)		
TiO_2	12	10 mg/L	125	125 W, UV	45	300	0.0019	[48]
ZnO	-	10 ppm	300	8 W, UV	51	60	0.0122	[49]
1% Ag-ZnO	-	10 ppm	300	8 W, UV	57	60	0.0143	[49]
3% Ag-ZnO	-	10 ppm	300	8 W, UV	54	60	0.0130	[49]
5% Ag-ZnO	-	10 ppm	300	8 W, UV	52	60	0.0122	[49]
SnO_2	12	2×10^{-5} M	1000	20 W, UV	100	600	0.008 ± 0.001	[50]
SnO_2: Zn^{2+}	2.4	2×10^{-5} M	1000	20 W, UV	100	80	0.040 ± 0.001	[50]
$CoWO_4$	30	5×10^{-5} M	2857	Visible	40	120	0.0033	[51]
$CuWO_4$	32	5×10^{-5} M	2857	Visible	70	120	0.0104	[51]
$ZnWO_4$	44	5×10^{-5} M	2857	Visible	95	120	0.0272	[51]
$CaWO_4$	32	1×10^{-5} M	1000	125 W, UV	94	60	0.0440	Present work
$SrWO_4$	33	1×10^{-5} M	1000	125 W, UV	74	60	0.0220	Present work
$BaWO_4$	55	1×10^{-5} M	1000	125 W, UV	100	60	0.0860	Present work

M = Ca, Sr and Ba

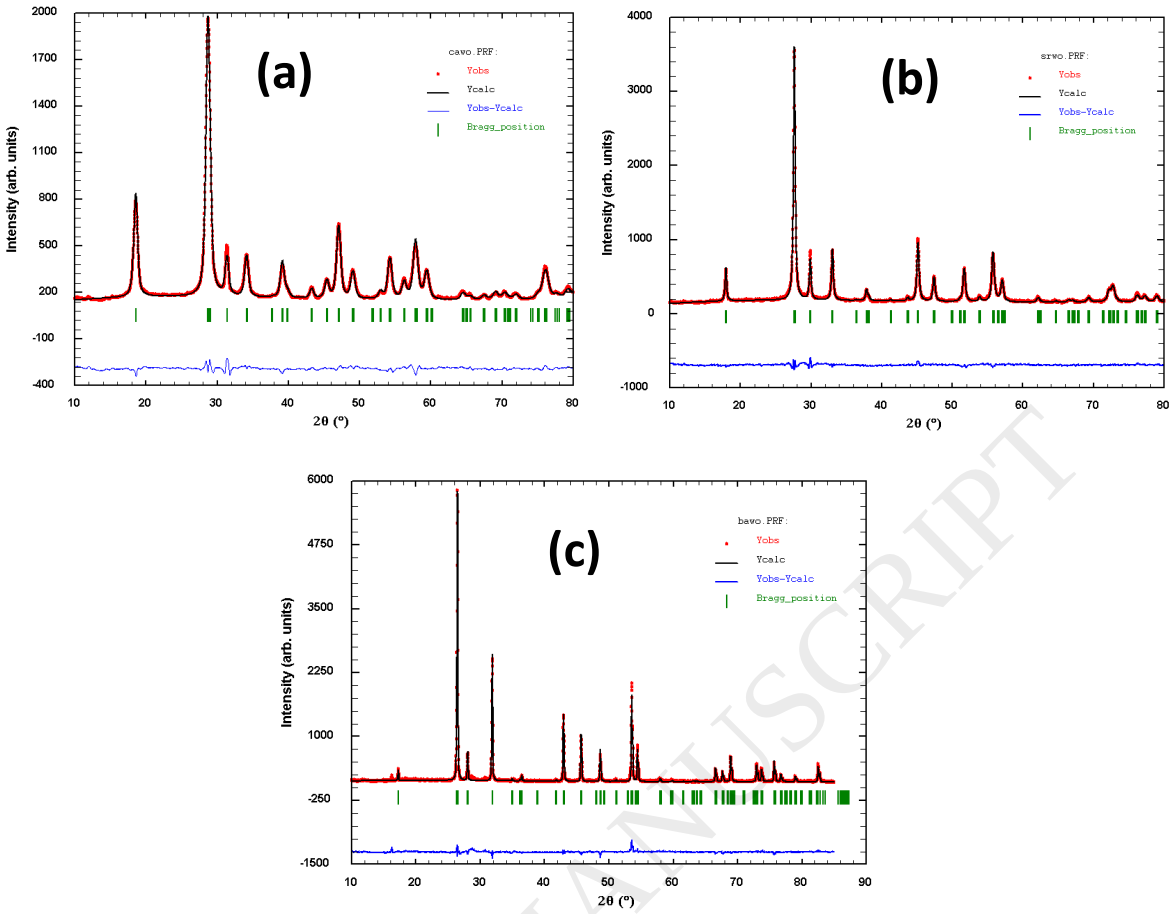

Fig. 1

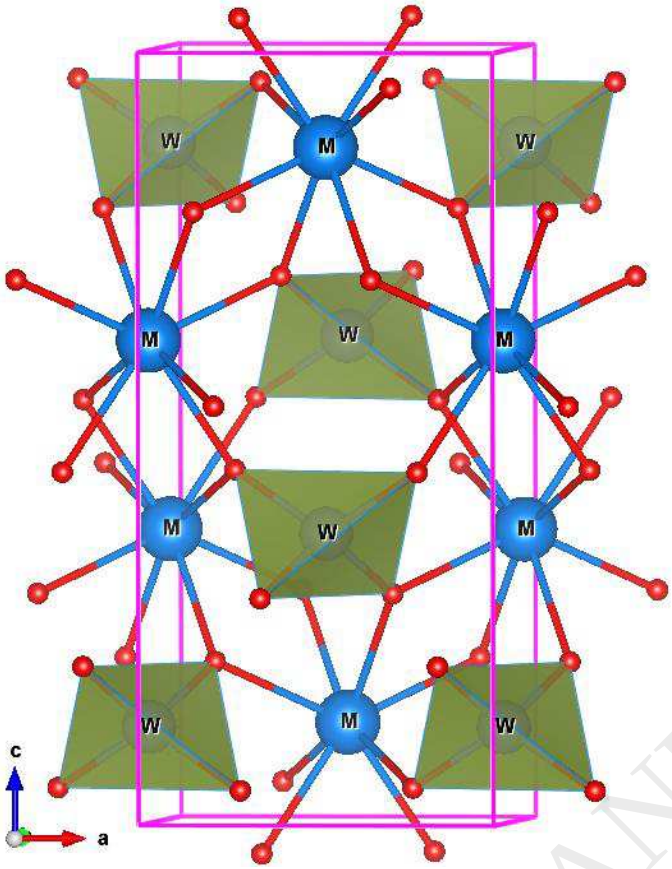

Fig. 2

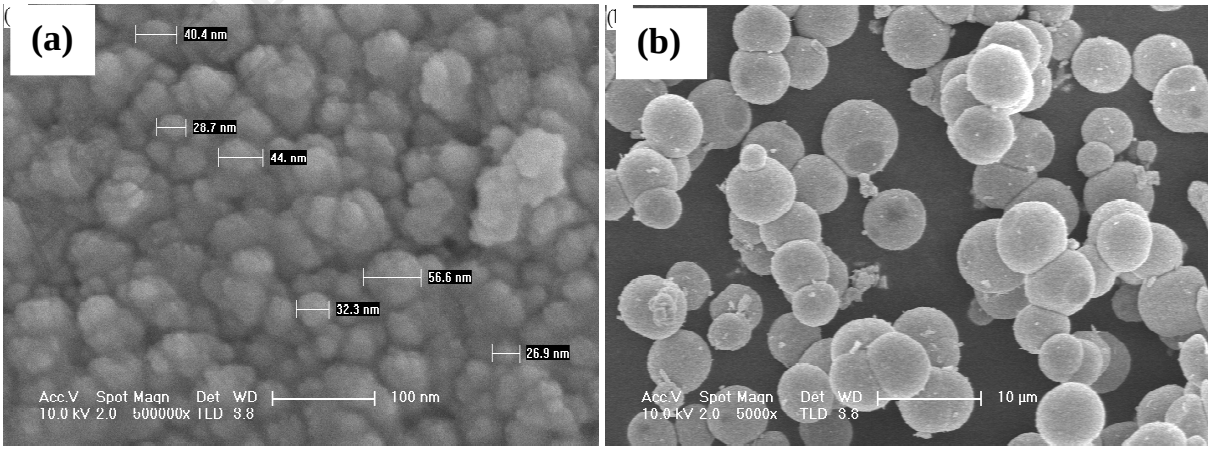

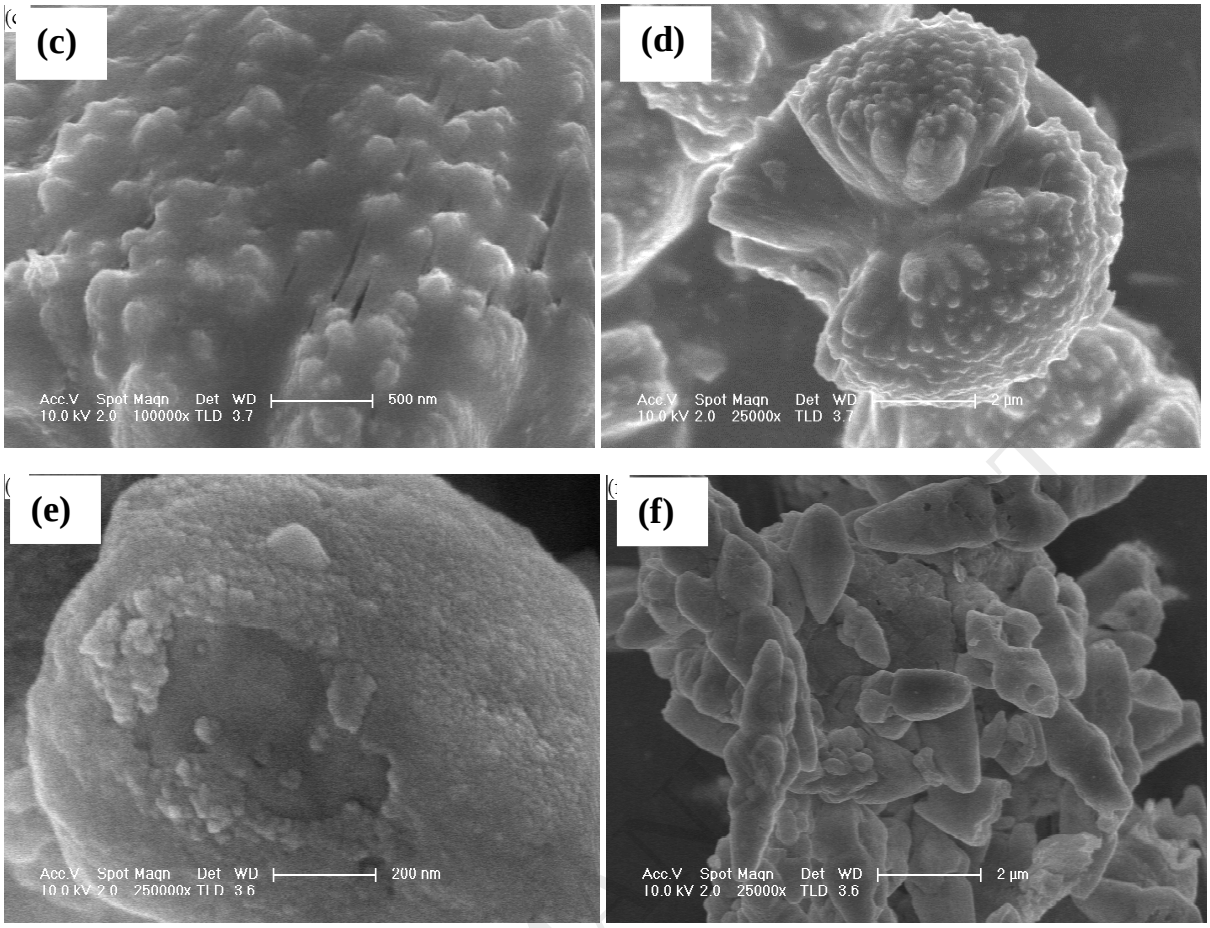

Fig. 3

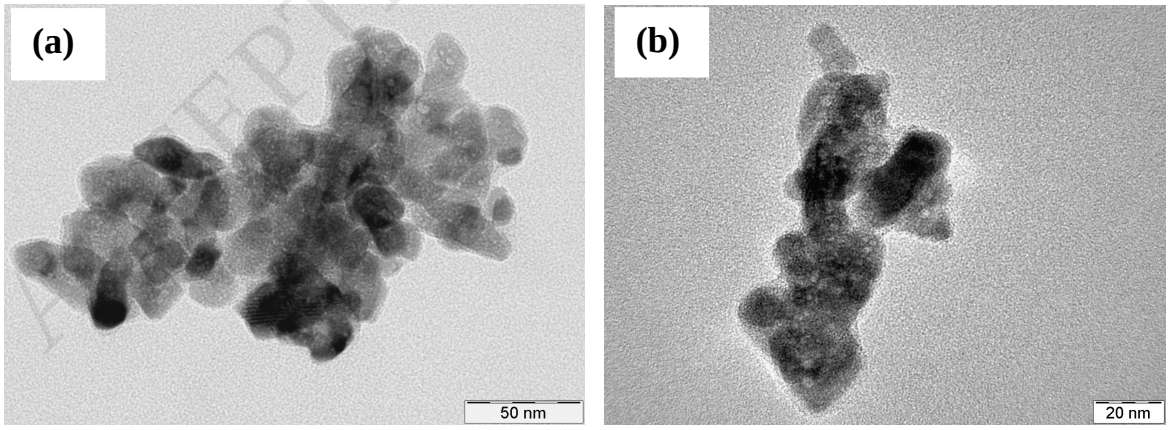

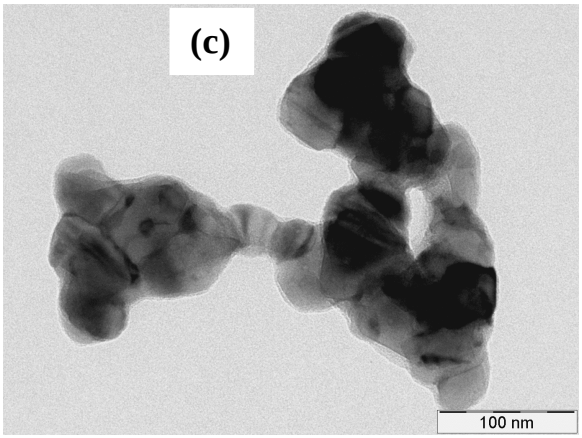

Fig. 4

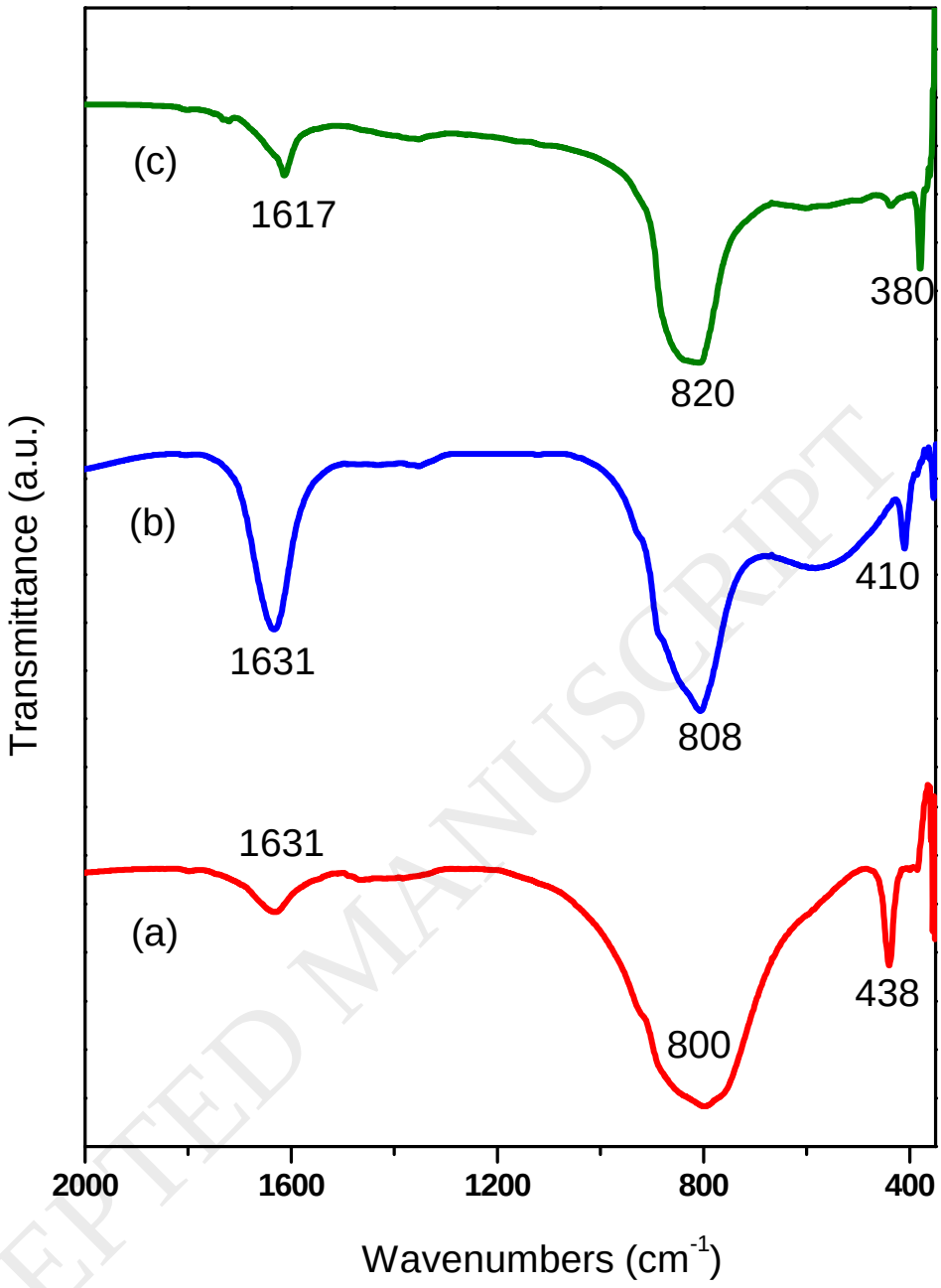

Fig. 5

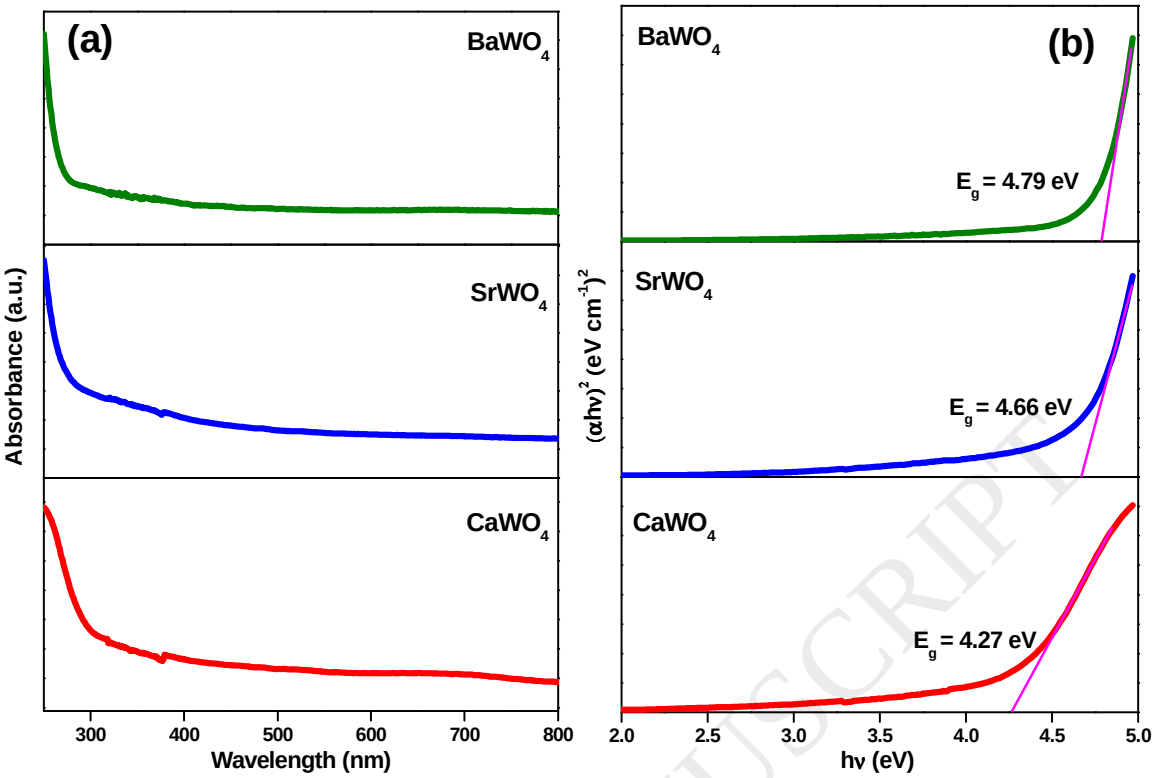

Fig. 6

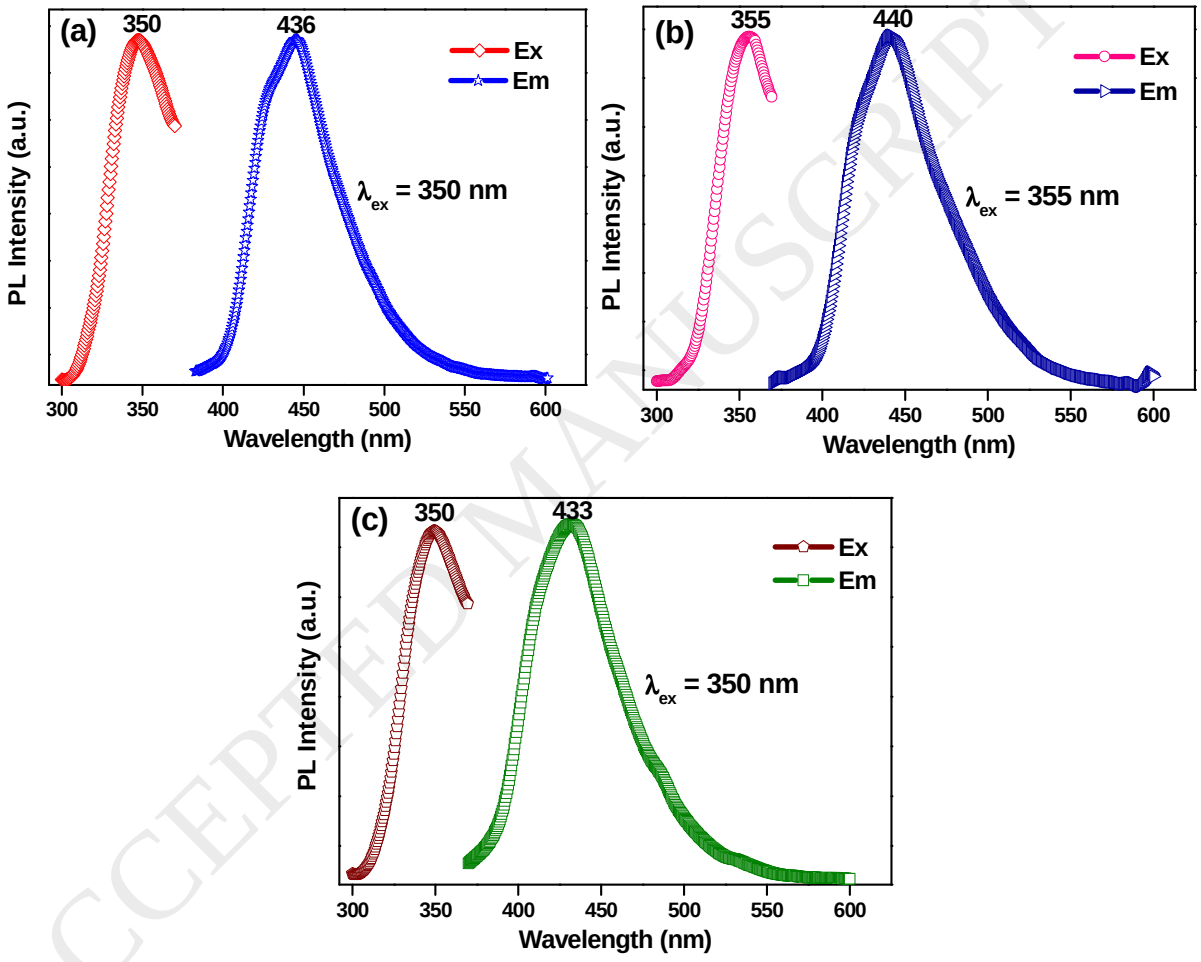

Fig. 7

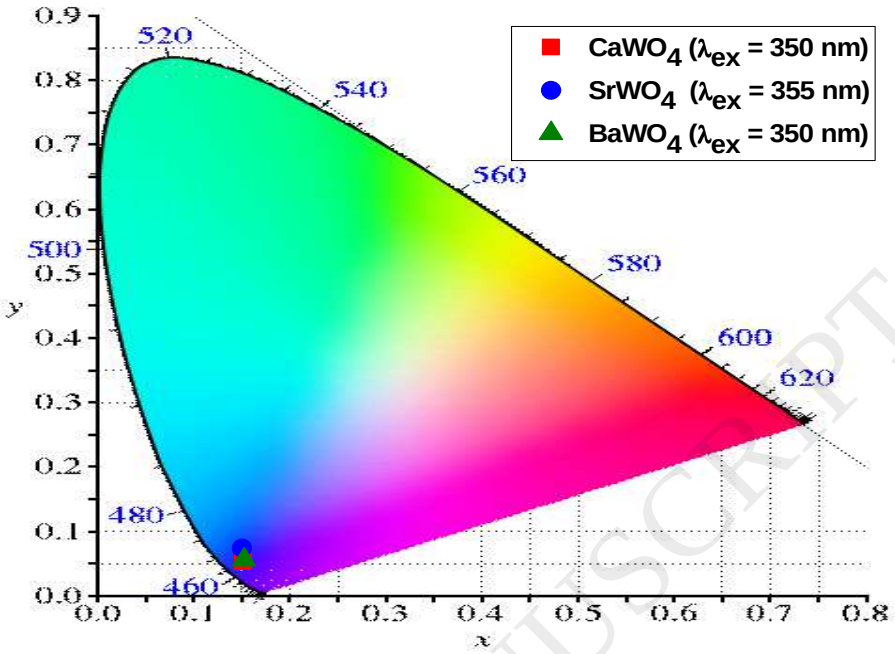

Fig. 8

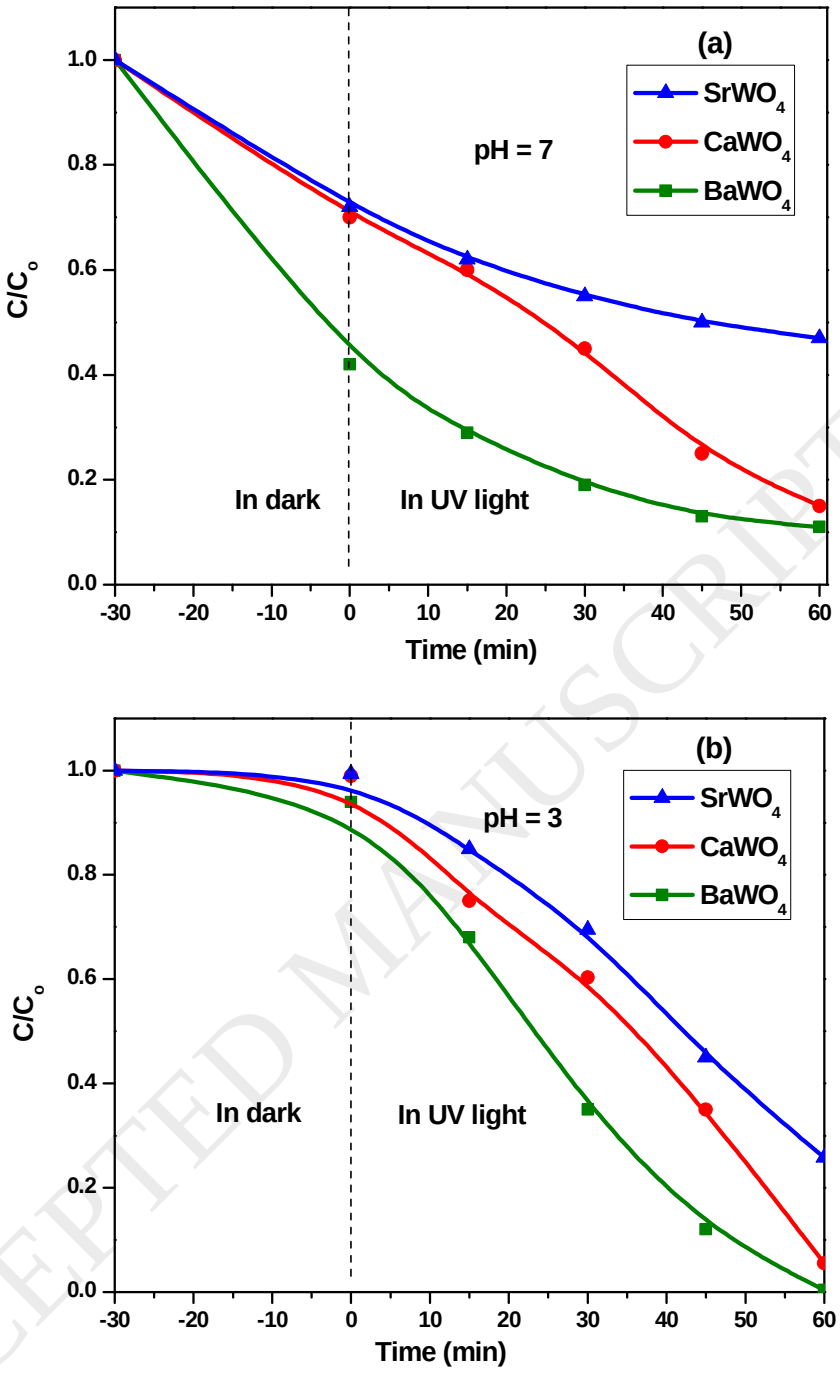

Fig. 9

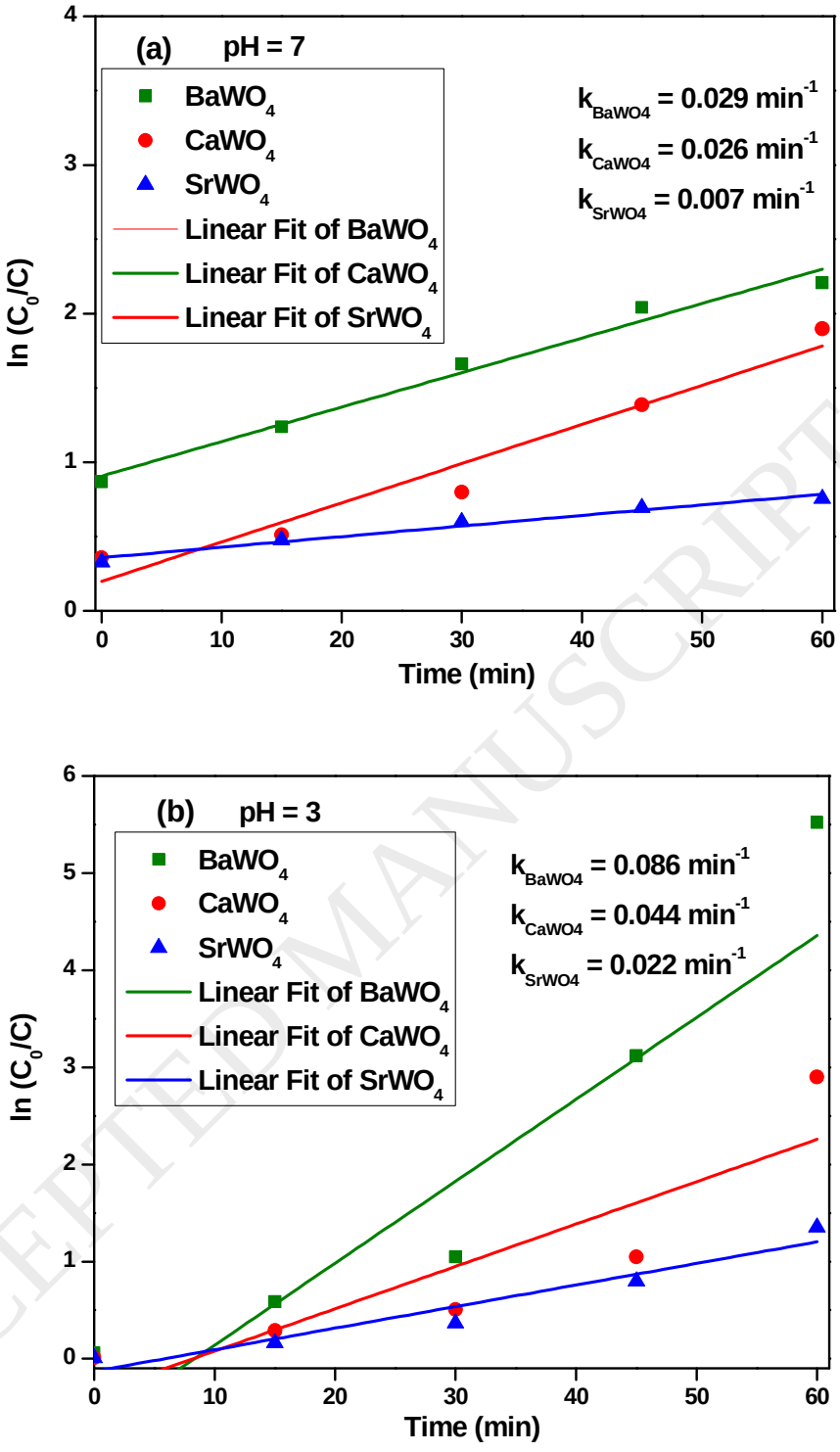

Fig. 10